Analysis of numerical solutions to Sommerfeld integral relation of the half-space radiator problem

Arun I, Murugesan Venkatapathi *

Computational and Statistical Physics Laboratory, Department of Computational Science, Indian Institute of Science, Bangalore - 560012, India

A B S T R A C T

Sommerfeld integrals relate a spherical wave from a point source to a convolution set of plane and cylindrical waves. This relation does not have analytical solutions but it submits to a solution by numerical integration. Among others, it is significant for theoretical studies of many optical and radiation phenomena involving surfaces. This approach is preferred over discretized computational models of the surface because of the many orders of increased computations involved in the latter. One of the most widely used and accurate methods to compute these solutions is the numerical integration of the Sommerfeld integrand over a complex contour. We have analyzed the numerical advantages offered by this method, and have justified the optimality of the preferred contour of integration and the choice of two eigenfunctions used. In addition to this, we have also analyzed four other approximate methods to compute the Sommerfeld integral and have identified their regions of validity, and numerical advantages, if any. These include the high relative permittivity approximation, the short distance approximation, the exact image theory and Fourier expansion of the reflection coefficient. We also finally compare these five methods in terms of their computational cost.

© 2016 IMACS. Published by Elsevier B.V. All rights reserved.

1. Introduction

The problem of modelling radiating antennas near a plane boundary such as the earth–air interface is of considerable practical importance in the fields of nano optics, oceanography, geophysical exploration, and submarine communication and detection. The radiation characteristics of an antenna can be substantially affected by the presence of a lossy ground with finite conductivity [4], especially in the near field of the antenna. Applications in nano optics also require the computation of interactions between a large number of dipole sources and substrates, thus requiring a repetitive use of this method numerous times to obtain a final solution of the problem [10,11,17,24,27,25,6,12,28]. Due to the vastly diminished scales involved in nano optics, the interaction between the dipole sources and the substrate is very significant [26,8,23].

The classic formulation of this problem by Sommerfeld [22,20,21] assumes a homogeneous lossy half-space with finite conductivity (say, the earth), and an infinitesimal vertical point dipole embedded in the free space (say, air) above it. Maxwell's equations are applied subject to the half-space boundary conditions, and the solutions are obtained in the form of an inverse Fourier–Bessel integral. This integral modelling the interaction of the dipole with the surface is known as the Sommerfeld integral. Since the problem has cylindrical symmetry, it is convenient to express the solution in cylindrical coordinates as an integral of the eigenfunctions of the cylindrical Helmholtz operator. These eigenfunctions are in terms

---

* Corresponding author.
  E-mail address: murugesh@cds.iisc.ac.in (M. Venkatapathi).

of the zeroth order Bessel function of the first kind for the ρ direction, and in terms of a complex exponential for the z direction. Because of the azimuthal symmetry in angle ϕ, the solutions are independent of ϕ.

The Sommerfeld integral has no closed form analytic solution, but there exist a few numerical methods to compute the solution. Since the integrand of the Sommerfeld integrand is oscillatory and has branch points along with other singularities, traditional numerical integration schemes converge poorly if the path of integration is not optimally chosen. Approximate analytic expressions can also be obtained when certain constraints are applied on the parameters. The objective of this work is to study the efficiency of the methods proposed so far, to evaluate the Sommerfeld integral in its amenable or approximated forms. Note that for more general scattering problems with arbitrarily shaped scatterers, other efficient integral equation solvers exist [3]. Similarly, these methods specific to this integral are expected to converge fast even if advanced numerical integration schemes designed for various types of singularities are not used. One method – exact image theory – is similar to integration schemes proposed for integrating functions with certain types of singularities [2,9,7,1]. The Sommerfeld integral based approach can in principle be combined with other integral equation solvers for problems involving an infinite surface and other scatterers [19].

The three spatial components of the vector potential for a z oriented oscillating electric point dipole in the near field of a surface are given in (1a) and (1b). The first two terms on the right hand side of (1a) represent the vector potential due to the primary dipole source and the image respectively. The third integral term is known as the Sommerfeld integral.

$$A_z = \frac{e^{ikR}}{R} + \frac{e^{ikR'}}{R'} - 2\int_0^\infty J_0(k_\rho \rho)e^{-k_z(z+h)}\frac{k_{zs}}{\varepsilon k_z + k_{zs}}\frac{k_\rho}{k_z}dk_\rho \tag{1a}$$

$$A_\rho = A_\phi = 0 \tag{1b}$$

$$k_z = \sqrt{k_\rho^2 - k^2} \tag{1c}$$

$$k_{zs} = \sqrt{k_\rho^2 - \varepsilon k^2} \tag{1d}$$

$$R = \sqrt{\rho^2 + (z-h)^2} \tag{1e}$$

$$R' = \sqrt{\rho^2 + (z+h)^2} \tag{1f}$$

where ε is the relative permittivity of the surface, k is the wave number in free space, k_ρ and k_z are the ρ and z components respectively of the wave number in free space, k_{zs} is the z component of the wave number under the surface, ρ and z are the coordinates of the observation point, and J_0 is the zeroth order Bessel function of the first kind.

Note the branch cuts and singularities of this integrand are shown in Fig. 1. We describe five methods to evaluate this integral; their regions of validity in terms of the permittivity of the half-space and the ρ/z ratios. Finally, in Section 7, we comment on the approximate computational costs involved in each of these methods.

2. Complex contour integration

For analytical integration, as a consequence of Cauchy's residue theorem, all different complex contours are equivalent provided the closed loop formed by the different contours of integration do not enclose any poles or singularities of the integrand and the contours do not intersect any branch cut of the integrand. However, numerical quadrature schemes would encounter oscillatory or non-oscillatory integrands depending on the contour chosen, and this can significantly affect the rate of convergence and accuracy of the numerical result.

2.1. Contour integration with Bessel functions

We start by ascertaining the location of the poles, branch points and branch cuts of the Sommerfeld integrand. The integrand has a pole p, given by (2), corresponding to $\varepsilon k_z + k_{zs} = 0$.

$$k_\rho = p = k\sqrt{\frac{\varepsilon}{1+\varepsilon}} \tag{2}$$

It also has branch points at $k_\rho = \pm k$ and $k_\rho = \pm k\sqrt{\varepsilon}$ due to $\sqrt{k_\rho^2 - k^2}$ and $\sqrt{k_\rho^2 - \varepsilon k^2}$ respectively. Choosing the conventional principal value of the square root function, the corresponding branch cuts are as given by (3). The detailed derivations which result in these branch cuts are shown in Appendix B.

$$k_\rho = t, \quad t \in [-k, k] \tag{3a}$$

$$k_\rho = it, \quad t \in \mathbb{R} \tag{3b}$$

$$k_\rho = t + i\frac{\varepsilon_y k^2}{2t}, \quad t \in \left[-k\Re\{\sqrt{\varepsilon}\}, k\Re\{\sqrt{\varepsilon}\}\right] \tag{3c}$$
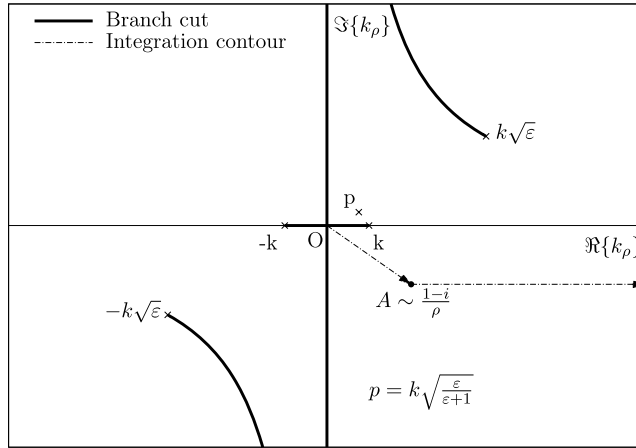
Fig. 1. Branch cuts and singularities of the Bessel function form of the Sommerfeld integrand in (1a). p refers to the location of the pole given by (2).
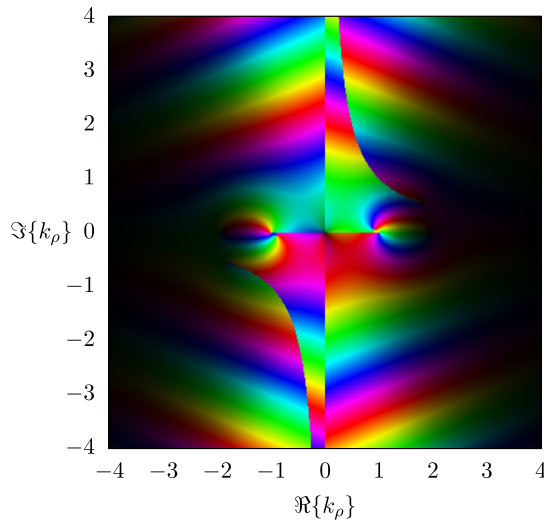

Fig. 2. Domain coloring visualization of the Bessel function form of the Sommerfeld integrand on the complex k_ρ plane for parameters $k = 1$, $\varepsilon = 3 + 2i$, $h = 1$, $\rho = 0.2\lambda$, $z = 0.4\lambda$ (See Appendix A for a quantitative description of domain coloring of complex valued functions).

These branch cuts are shown in Fig. 1 and may also be seen in the domain coloring visualization of the Sommerfeld integrand shown in Fig. 2. The preferred contour of integration due to Lytle and Lager [16], that avoids the branch cuts and singularities discussed above is also shown in Fig. 2. Point A in the preferred contour of integration is chosen to be

$$A \sim \frac{1-i}{\rho} \tag{4}$$

The Bessel function term in the integrand increases exponentially in the lower half of the complex plane. So, to avoid large cancellation errors, the contour is chosen such that the argument of the Bessel function $k_\rho \rho$ remains roughly constant for different values of ρ. Hence, we have the $\frac{1}{\rho}$ term in A. The slope of OA given by the $1 - i$ in the numerator is arbitrary.

A comparison of the number of integrand evaluations required for convergence in the case of integration over the real line and integration over the complex contour is shown in Fig. 3. Integration over the real line requires several orders of magnitude more number of integrand evaluations than the contour integration. Thus, it is clear from these numerical results, that contour integration has a significant computational advantage. Note that, to estimate the computational cost of real line integration, a contour arbitrarily close to the real line was chosen. This is because a contour over the real line will converge very poorly due to the singularities on the real line.
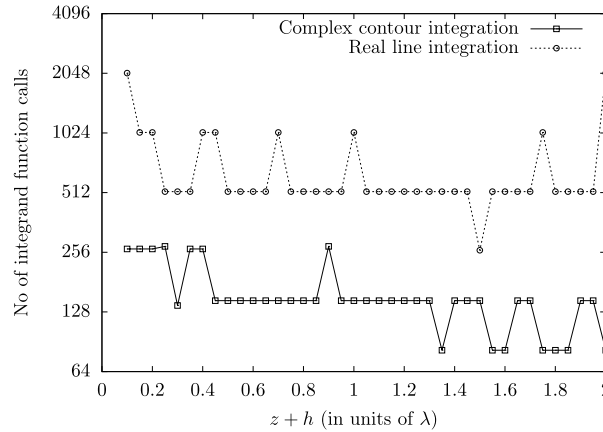
Fig. 3. Comparison of computational cost of integration over the real line and over the contour (for parameters $k = 1$, $\varepsilon = 7 + 3i$, $\rho = 0.35\lambda$). The computational cost of real line integration involves a contour arbitrarily close to the real line.
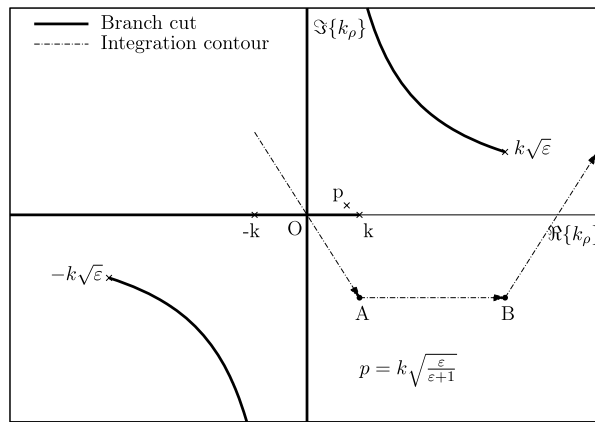

Fig. 4. Branch cuts and singularities of the Hankel function form of the Sommerfeld integrand. p refers to the location of the pole given by (2).

2.2. Contour integration with Hankel functions

The Bessel function form of the Sommerfeld integral has limits from 0 to ∞, whereas the equivalent integral using Hankel functions [22] has limits from $-\infty$ to ∞, as follows.

$$\int_0^\infty J_0(k_\rho\rho)e^{-k_z(z+h)}\frac{k_z}{\varepsilon k_z + k_{zs}}\frac{k_\rho}{k_z}\mathrm{d}k_\rho = \frac{1}{2}\int_{-\infty}^\infty H_0^1(k_\rho\rho)e^{-k_z(z+h)}\frac{k_z}{\varepsilon k_z + k_{zs}}\frac{k_\rho}{k_z}\mathrm{d}k_\rho \tag{5}$$

where H_0^1 is the zeroth order Hankel function of the first kind.

In addition to the branch cuts of the Bessel function form of the Sommerfeld integrand, the Hankel function form of the Sommerfeld integrand has an additional branch cut along the negative real axis due to the Hankel function. This branch cut is given by

$$k_\rho = t \in (-\infty, 0] \tag{6}$$

The branch cuts of the Hankel function form of the Sommerfeld integrand along with the preferred contour of integration are shown graphically in Fig. 4. Points A and B in the preferred contour of integration are given by

$$A \sim \frac{z - i\rho}{\rho} \tag{7}$$

$$B = k\Re\{\sqrt{\varepsilon}\} + \Im\{A\} \tag{8}$$

The Hankel function term in the integrand increases exponentially in the lower half of the complex plane. So, to avoid large cancellation errors, the contour is chosen such that the argument of the Hankel function $k_\rho\rho$ remains roughly constant for different values of ρ. Hence, we have the $\frac{1}{\rho}$ term in A. The slope of OA given by the $z - i\rho$ is chosen to approximate a
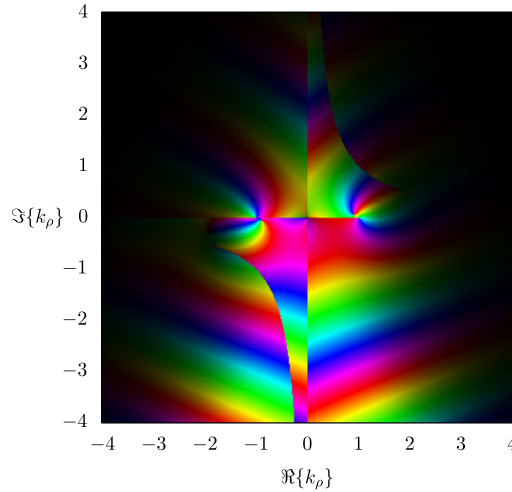
Fig. 5. Domain coloring visualization of the Hankel function form of the Sommerfeld integrand on the complex k_ρ plane for parameters $k = 1$, $\varepsilon = 3 + 2i$, $h = 1$, $\rho = 0.2\lambda$, $z = 0.4\lambda$ (See Appendix A for a quantitative description of domain coloring of complex valued functions).

contour corresponding to constant phase of the integrand. Smaller phase variations along the contour result in the numerical quadrature scheme encountering a less oscillatory integrand, and hence this is preferred. Point B is chosen such that when the contour returns to the upper half of the complex plane, it does not intersect the branch cut due to $k_{zs} = \sqrt{k_\rho^2 - \varepsilon k^2}$.

The Bessel function form of the Sommerfeld integrand suffers from rapid oscillations for large ρ and slow decay for small $z + h$. Hence, for observation points along the planar interface and distant from the source, convergence is slow. In these cases, the Hankel function form of the integrand, which does not suffer from these issues, can be used. The infinite range of integration can be truncated to a relatively short range because of the fact that the Hankel function decays exponentially in the upper half of the complex plane. A domain coloring visualization of the Hankel function form of the Sommerfeld integrand is shown in Fig. 5.

3. High relative permittivity approximation

In his original work [22], Sommerfeld developed the following approximate image theory for surfaces of high permittivity.

$$A_z = \int_0^\infty J_0(k_\rho \rho) e^{-k_z(z+h)} \frac{k_{zs}}{\varepsilon k_z + k_{zs}} \frac{k_\rho}{k_z} dk_\rho \tag{9}$$

For infinitely large ε, the Sommerfeld integral vanishes. For large but not infinitely large ε, an useful limit case can be derived. This is as follows.

The z component of the wave number under the surface k_{zs} is given by

$$k_{zs} = \sqrt{k_\rho^2 - \varepsilon k^2} \tag{10}$$

$$k_{zs} = \sqrt{\varepsilon} k \sqrt{\frac{k_\rho^2}{\varepsilon k^2} - 1} \tag{11}$$

For large ε, that is, $\sqrt{\varepsilon} k \gg k_\rho$

$$k_{zs} = -ik\sqrt{\varepsilon} \tag{12}$$

Also, in the denominator,

$$\varepsilon k_z + k_{zs} \approx \varepsilon k_z \tag{13}$$

Applying approximations (12) and (13),

$$A_z = -\frac{ik}{\sqrt{\varepsilon}} \int_0^\infty J_0(k_\rho \rho) e^{-k_z(z+h)} \frac{k_\rho}{k_z^2} dk_\rho \tag{14}$$

This approximate integral can be interpreted as an image theory in the following way.

For $R'' = \sqrt{\rho^2 + (z + h')^2}$, the Fourier–Bessel integral of the free-space Green's function can be expressed as
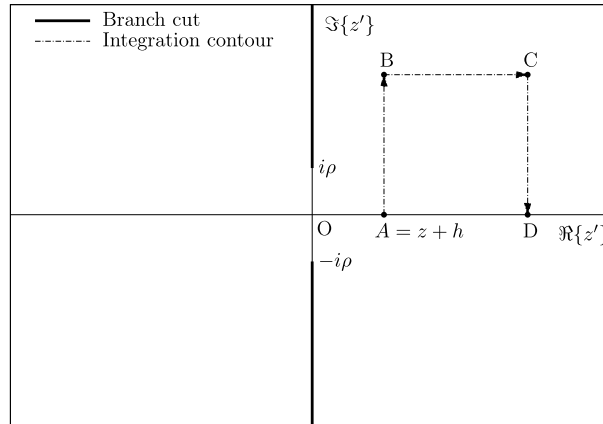
Fig. 6. Branch cuts and singularities of the high relative permittivity integrand.

$$\frac{e^{ikR''}}{R''} = \int_0^\infty J_0(k_\rho \rho) e^{-k_z(z+h')} \frac{k_\rho}{k_z} dk_\rho \tag{15}$$

Integrating with respect to h' from h to ∞,

$$\int_h^\infty \frac{e^{ikR''}}{R''} dh' = \int_0^\infty J_0(k_\rho \rho) e^{-k_z z} \frac{k_\rho}{k_z} dk_\rho \int_h^\infty e^{-k_z h'} dh' \tag{16}$$

$$\int_h^\infty \frac{e^{ikR''}}{R''} dh' = \int_0^\infty J_0(k_\rho \rho) e^{-k_z z} \frac{k_\rho}{k_z^2} dk_\rho \tag{17}$$

Thus,

$$A_z = -\frac{ik}{\sqrt{\varepsilon}} \int_h^\infty \frac{e^{ikR''}}{R''} dh' \tag{18}$$

$$A_z = -\frac{ik}{\sqrt{\varepsilon}} \int_{z+h}^\infty \frac{e^{ikR''}}{R''} dz' \tag{19}$$

where $z' = z + h'$ and $R'' = \sqrt{\rho^2 + (z')^2}$

This can be interpreted as the effect of an imaginary ray of dipoles starting at $z = -h$ and going to $z = -\infty$.

The high permittivity integrand shown in (19) has branch cuts due to the square root function in $R'' = \sqrt{\rho^2 + (z')^2}$. Choosing the conventional principal value of the square root function, the branch cut is

$$z' = \pm it, \quad t \in [\rho, \infty) \tag{20}$$

The detailed derivation which results in this branch cut is shown in Appendix C. The branch point corresponding to this branch cut is at

$$z' = \pm i\rho \tag{21}$$

For the high permittivity integrand, contours parallel to the imaginary axis in the z' plane encounter an exponentially decaying integrand. But, contours parallel to the real axis in the z' plane encounter an oscillatory integrand. Also, as the magnitude of z' tends to infinity, the integrand approaches zero. Hence, for rapid convergence with numerical integration, we choose a contour as shown in Fig. 6.

When $|B| \to \infty$, $|C| \to \infty$ and $|D| \to \infty$, the integrand decays to a negligible value at points B, C and D, and therefore contour AB approximates contour $ABCD$. Note that $\lim_{z' \to \infty} R'' = z'$.

$$\int_{z+h}^\infty \frac{e^{ikR''}}{R''} dz' = \int_{ABCD} \frac{e^{ikR''}}{R''} dz' \approx \int_{AB} \frac{e^{ikR''}}{R''} dz' \tag{22}$$
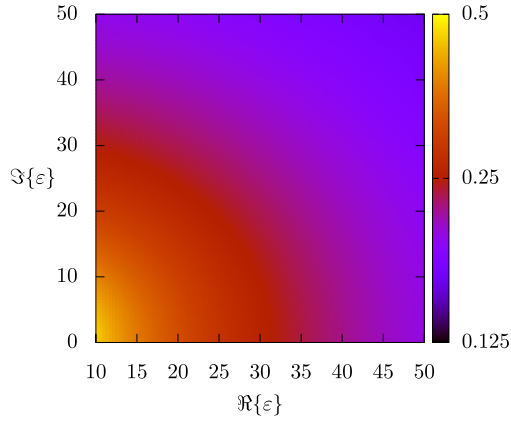
Fig. 7. High permittivity approximation versus complex contour integration – Relative error (for parameters $k = 1$, $\rho = 2\lambda$ and $z = 2\lambda$).

3.1. Error analysis

The relative error in the integrand caused by approximation (12) is given by

$$\text{Relative error in integrand} = 1 + i\sqrt{\varepsilon}\frac{k}{k_{zs}} = 1 + ik\sqrt{\frac{\varepsilon}{k_\rho^2 - \varepsilon k^2}} \tag{23}$$

The relative error in the integrand caused by approximation (13) is given by

$$\text{Relative error in integrand} = \frac{k_{zs}}{\varepsilon k_z} = \frac{1}{\varepsilon}\sqrt{\frac{k_\rho^2 - \varepsilon k^2}{k_\rho^2 - k^2}} \tag{24}$$

Putting both approximations (12) and (13) together, the relative error is given by

$$\text{Relative error in integrand} = \frac{-ik}{\sqrt{\varepsilon}k_z}\left(1 + \frac{\varepsilon k_z}{k_{zs}}\right) \tag{25}$$

$$\text{Relative error in integrand} = \frac{k}{i\sqrt{\varepsilon}}\left(\frac{1}{k_z} + \frac{\varepsilon}{k_{zs}}\right) \tag{26}$$

$$\text{Relative error in integrand} = \frac{k}{i\sqrt{\varepsilon}}\left(\frac{1}{\sqrt{k_\rho^2 - k^2}} + \frac{\varepsilon}{\sqrt{k_\rho^2 - \varepsilon k^2}}\right) \tag{27}$$

This relative error in the integrand given by (27) shows maxima at $k_\rho = k$ and $k_\rho = k\sqrt{\varepsilon}$. Therefore, the high permittivity approximation will show smaller error for parameters whose corresponding integrands only have a small component at these points in the complex k_ρ plane. Since all contours in the complex plane are equivalent, the error in the final result cannot be minimized by choosing a contour of integration that avoids these points. A comparison of the relative error for the high permittivity approximation versus complex contour integration for different values of relative permittivity is shown in Fig. 7. As can be seen, the approximation becomes more accurate for larger permittivities.

4. Short distance approximation

This approximation due to Panasyuk et al. [18] is applicable when the observation point is close to the reflection of the dipole source about the planar interface, that is for small kL where $L = \sqrt{\rho^2 + (z + h)^2}$ is the distance between the observation point and the reflection of the dipole source about the planar interface.

Detailed derivation of the results of the short distance approximation are shown in [18]. Here, we will consider only the approximations used and the region of validity of these approximations.

One of the forms of the Sommerfeld integral dealt with in this approximation is

$$I = \int_0^\infty J_0(k_\rho \rho)e^{-k_z(z+h)}\frac{k_{zs} - \varepsilon k_z}{k_{zs} + \varepsilon k_z}\frac{k_\rho^3}{k_z}dk_\rho \tag{28}$$

The integral is first split into three parts

$$I = \int\limits_0^k f(k_\rho) J_0(k_\rho \rho) e^{-k_z(z+h)} \mathrm{d}k_\rho + \int\limits_k^\infty [f(k_\rho) - g(k_\rho)] J_0(k_\rho \rho) e^{-k_z(z+h)} \mathrm{d}k_\rho + \int\limits_k^\infty g(k_\rho) J_0(k_\rho \rho) e^{-k_z(z+h)} \mathrm{d}k_\rho \quad (29)$$

where

$$f(k_\rho) = \frac{k_\rho^3}{k_z} \frac{k_{zs} - \varepsilon k_z}{k_{zs} + \varepsilon k_z} \tag{30}$$

$$g(k_\rho) = \frac{k_\rho^3}{k_z} \left[s + \frac{s(1-s)k^2}{2k_\rho^2} \right] \tag{31}$$

$$s = \frac{1 - \varepsilon}{1 + \varepsilon} \tag{32}$$

Then, the variable of integration is transformed with $\xi = \sqrt{1 - \left(\frac{k_\rho}{k}\right)^2}$ in the first integral, and $\xi = \sqrt{\left(\frac{k_\rho}{k}\right)^2 - 1}$ in the last two integrals, resulting in integrals t_1, t_2 and t_3.

$$I = k^3 [it_1 + t_2 + t_3] \tag{33}$$

where

$$t_1 = \int\limits_0^1 (1 - \xi^2) J_0(k\rho\sqrt{1 - \xi^2}) e^{i\xi k(z+h)} Q_1(\xi) \mathrm{d}\xi \tag{34}$$

$$t_2 = \int\limits_0^\infty (1 + \xi^2) J_0(k\rho\sqrt{1 + \xi^2}) e^{-\xi k(z+h)} \left[Q_2(\xi) - s - \frac{s(1-s)}{2(1+\xi^2)} \right] \mathrm{d}\xi \tag{35}$$

$$t_3 = \int\limits_0^\infty (1 + \xi^2) J_0(k\rho\sqrt{1 + \xi^2}) e^{-\xi k(z+h)} \left[s + \frac{s(1-s)}{2(1+\xi^2)} \right] \mathrm{d}\xi \tag{36}$$

$$Q_1(\xi) = \frac{\sqrt{\xi^2 + \varepsilon - 1} - \varepsilon\xi}{\sqrt{\xi^2 + \varepsilon - 1} + \varepsilon\xi} \tag{37}$$

$$Q_2(\xi) = \frac{\sqrt{\xi^2 - \varepsilon + 1} - \varepsilon\xi}{\sqrt{\xi^2 - \varepsilon + 1} + \varepsilon\xi} \tag{38}$$

Now, suitable short distance approximations are applied on integrals t_1, t_2 and t_3. These approximations make the integrals analytically integrable and result in the expressions shown in (42), (43) and (54). The region of validity of these approximations is discussed here.

In integrals t_1 and t_2, the Bessel function terms and the exponential terms are approximated by unity, which is the first term in their respective Taylor series.

$$J_0(k\rho\sqrt{1 - \xi^2}) \approx 1 \tag{39a}$$

$$J_0(k\rho\sqrt{1 + \xi^2}) \approx 1 \tag{39b}$$

$$e^{i\xi k(z+h)} \approx 1 \tag{39c}$$

$$e^{-\xi k(z+h)} \approx 1 \tag{39d}$$

The approximations in (39) are valid only for very small arguments of the exponential and Bessel functions. Therefore, $k\rho$ and $k(z+h)$ are required to be very small quantities. Thus, this approximation is valid only when ρ and $z+h$ are much smaller than the free space wavelength λ.

$$\rho \ll \lambda \tag{40}$$

$$z + h \ll \lambda \tag{41}$$

Substituting these approximations into (34) and (35), and evaluating the resulting integrals analytically results in (42) and (43) for integrals t_1 and t_2 respectively.

$$
t_1 = -\frac{2\sqrt{\varepsilon - 1}}{(\varepsilon - 1)(\varepsilon + 1)^2} \left\{ \left[\varepsilon(1 + 3\varepsilon - \varepsilon^2) + \sqrt{\varepsilon - 1} \left(\frac{\varepsilon^{\frac{5}{2}}(\sqrt{\varepsilon} + 2)}{\sqrt{\varepsilon} + 1} - 2\varepsilon - 1 \right) \right] \right\}
$$
$$
- \frac{6\varepsilon^3}{(\varepsilon - 1)(\varepsilon + 1)^{2.5}} \ln \left[\frac{(\varepsilon + \sqrt{\varepsilon^2 - 1})(1 + \sqrt{\varepsilon + 1})}{\varepsilon + \sqrt{\varepsilon(\varepsilon + 1)}} \right] \tag{42}
$$

$$
t_2 = \frac{\varepsilon}{(1 + \varepsilon)^{1.5}} \left[\pi + \frac{2\sqrt{1 - \varepsilon^2}}{3} + \frac{\pi + 2i\varepsilon^2 \ln[i\varepsilon + \sqrt{1 - \varepsilon^2}] - 2\varepsilon\sqrt{1 - \varepsilon^2}}{\varepsilon^2 - 1} \right] \tag{43}
$$

In integral t_3, the argument of the Bessel function grows linearly with the integration variable ξ at the upper limit of integration. Hence, direct approximation using the Taylor series is not possible. Hence, we make the argument of the Bessel function bounded as follows.

$$J_0(k\rho\sqrt{1 + \xi^2}) = J_0[k\rho(\xi + \Delta\xi)] \tag{44}$$

where

$$\Delta\xi = \sqrt{1 + \xi^2} - \xi \tag{45}$$

Then, using the addition theorem for Bessel functions,

$$J_0(k\rho\sqrt{1 + \xi^2}) = \sum_{n=-\infty}^{\infty} J_{-n}(k\rho\xi) J_n(k\rho\Delta\xi) \tag{46}$$

Truncating the series due to the addition theorem at $n = 1$,

$$
\begin{aligned}
J_0(k\rho\sqrt{1 + \xi^2}) &= J_1(k\rho\xi) J_{-1}(k\rho\Delta\xi) \\
&\quad + J_0(k\rho\xi) J_0(k\rho\Delta\xi) \\
&\quad - J_{-1}(k\rho\xi) J_1(k\rho\Delta\xi)
\end{aligned} \tag{47}
$$

For Bessel functions of integer order n,

$$J_{-n}(z) = (-1)^n J_n(z) \tag{48}$$

Therefore,

$$J_0(k\rho\sqrt{1 + \xi^2}) = J_0(k\rho\xi) J_0(k\rho\Delta\xi) - 2J_1(k\rho\xi) J_1(k\rho\Delta\xi) \tag{49}$$

Now, that the argument $k\rho\Delta\xi$ is bounded, we can approximate it using the first term of the Taylor series as follows.

$$J_0(k\rho\Delta\xi) \approx 1 \tag{50}$$

$$J_1(k\rho\Delta\xi) \approx \frac{k\rho\Delta\xi}{2} \tag{51}$$

Substituting these approximations, we obtain,

$$J_0(k\rho\sqrt{1 + \xi^2}) = J_0(k\rho\xi) - k\rho\Delta\xi J_1(k\rho\xi) \tag{52}$$

Analogous to the approximations in (39), this approximation using the Taylor series is valid only for very small values of $k\rho$, that is, when ρ is much smaller than the free space wavelength λ.
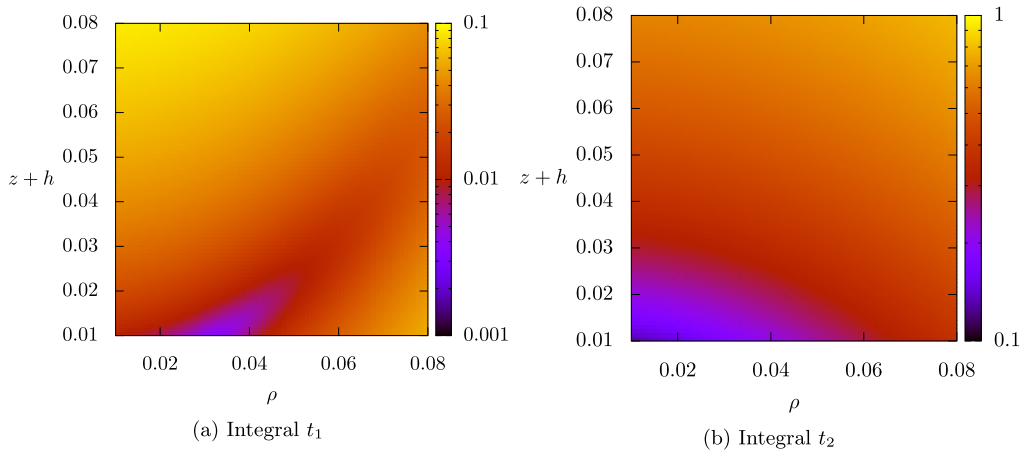
$$\rho \ll \lambda \tag{53}$$

(a) Integral t_1 (b) Integral t_2

Fig. 8. Short distance approximation versus complex contour integration – Relative error for a $\rho \times z$ grid (for parameters $k = 1$, $\varepsilon = 3 + 2i$).

Substituting approximation (52) into (36), and evaluating the resulting integrals analytically results in (54) for integral t_3.

$$t_3 = \frac{s}{(kL)^3}\left[3\left(\frac{z+h}{L}\right)^2 - 1\right] - \frac{1}{kL}\left[s + \frac{s(1-s)}{2} - \frac{sR^2}{2kL^3}\right] \tag{54}$$

4.1. Error analysis

$$\text{Absolute error in } t_1 = \int_0^1 (1-\xi^2)J_0(k\rho\sqrt{1-\xi^2})e^{i\xi k(z+h)}Q_1(\xi)\mathrm{d}\xi - \int_0^1 (1-\xi^2)Q_1(\xi)\mathrm{d}\xi \tag{55}$$

$$\text{Absolute error in } t_1 = \int_0^1 (1-\xi^2)\left[J_0(k\rho\sqrt{1-\xi^2})e^{i\xi k(z+h)} - 1\right]Q_1(\xi)\mathrm{d}\xi \tag{56}$$

$$\text{Absolute error in } t_2 = \int_0^\infty (1+\xi^2)\left[J_0(k\rho\sqrt{1+\xi^2})e^{-\xi k(z+h)} - 1\right]\left[Q_2(\xi) - s - \frac{s(1-s)}{2(1+\xi^2)}\right]\mathrm{d}\xi \tag{57}$$

Since, in approximation (39), the oscillatory terms – namely the Bessel and exponential functions – where replaced by unity, the error introduced is also oscillatory. This is shown in the above expressions.

4.2. Numerical results

Numerical results computing the relative error of the short distance approximation for integrals t_1 and t_2 are shown in Fig. 8. As can be seen from the figures, the error does not monotonically increase with increasing distance from the reflected source. Instead, there is an oscillating variation in the error. The source of this oscillating error is due to approximation by substitution of oscillatory terms in the integrand with constant terms, as explained in the previous section.

4.3. Observations and conclusions

When the observation point is very close to the reflected source point, numerical integration of the Sommerfeld integral converges slowly. In such cases, this short distance approximation is useful. Also, when approximate analytical results are required, this short distance approximation provides a more accurate alternative to the well known electrostatic approximation. However, as an accurate general purpose numerical technique for all observation points, this approximation will not suffice.

5. Exact image theory

An exact distributed image current function for the classical Sommerfeld half-space problem was obtained by Lindell and Alanen for excitation by a vertical magnetic dipole [13], a vertical electric dipole [14], and for arbitrarily oriented electric or magnetic dipoles [15]. We shall only consider excitation by a vertical electric dipole.

The vector potential $A(\mathbf{r})$ possesses only a z component and satisfies the Helmholtz wave equation, given by

$$(\nabla^2 + k^2)A(\mathbf{r}) = -\delta(\mathbf{r} - h\hat{\mathbf{z}}), \qquad z > 0 \tag{58}$$

$$(\nabla^2 + \varepsilon k^2)A(\mathbf{r}) = 0, \qquad z < 0 \tag{59}$$

The Fourier transform of the solution can be written as

$$A_z(k_\rho) = \frac{J_0(k_\rho \rho)}{k_z}\left[e^{-k_z(z-h)} + R_e e^{-k_z(z+h)}\right], \quad z > 0 \tag{60}$$

where R_e is the reflection coefficient given by

$$R_e(k_z) = \frac{\varepsilon k_z - k_{zs}}{\varepsilon k_z + k_{zs}} \tag{61}$$

(60) can be split into two terms A_1 and A_2 as

$$A_z = A_1 + A_2 \tag{62}$$

where

$$A_1(k_\rho) = \frac{J_0(k_\rho \rho)}{k_z}e^{-k_z(z+h)} \tag{63}$$

$$A_2(k_\rho) = \frac{J_0(k_\rho \rho)}{k_z}R_e e^{-k_z(z+h)} \tag{64}$$

A_1 corresponds to the field due to a vertical electric dipole at $z = h$ radiating in free space. In the space domain,

$$A_1(\mathbf{r}) = G(\mathbf{r} - h\hat{\mathbf{z}}) \tag{65}$$

where $G(\mathbf{r})$ is the free space Green's function given by

$$G(\mathbf{r}) = \frac{e^{-ikr}}{4\pi r} \tag{66}$$

A_2 corresponds to the field due to reflection from the surface. $A_2(k_\rho)$ is the reflected field due to an incident wave with wave number $\mathbf{k} = k_\rho \boldsymbol{\rho} + k_z \hat{\mathbf{z}}$

Now, we try to express A_2 as some superposition of point sources radiating in homogeneous space. For this, we first normalize the propagation factor k_z using $q = \frac{k_z}{ik\sqrt{\varepsilon - 1}}$ to get

$$R_e(q) = \frac{\varepsilon q - \sqrt{q^2 + 1}}{\varepsilon q + \sqrt{q^2 + 1}} \tag{67}$$

If f is the Laplace transform of the reflection coefficient $R_e(q)$, then

$$R_e(q) = \int\limits_0^\infty f(p)e^{-qp}\mathrm{d}p \tag{68}$$

Substituting this Laplace representation of $R_e(q)$ into (64),

$$A_2(k_\rho) = -\frac{J_0(k_\rho \rho)}{k_z}e^{-k_z(z+h)}\int\limits_0^\infty f(p)e^{-pq}\mathrm{d}p \tag{69}$$

Inverting the Fourier transform,

$$A_2(k_\rho) = \int\limits_0^\infty J_0(k_\rho \rho)e^{-k_z(z+h)}\frac{k_\rho}{k_z}\int\limits_0^\infty f(p)e^{-pq}\mathrm{d}p\,\mathrm{d}k_\rho \tag{70}$$

Swapping the order of the integrals,

$$A_2(k_\rho) = \int\limits_0^\infty f(p)\int\limits_0^\infty J_0(k_\rho \rho)e^{-k_z(z+h)}e^{-pq}\frac{k_\rho}{k_z}\mathrm{d}k_\rho\,\mathrm{d}p \tag{71}$$

Substituting $q = \frac{k_z}{ik\sqrt{\varepsilon - 1}}$,

$$A_2(k_\rho) = \int\limits_0^\infty f(p) \int\limits_0^\infty J_0(k_\rho \rho) e^{-k_z\left[z+h+\frac{p}{ik\sqrt{\varepsilon-1}}\right]} \frac{k_\rho}{k_z} \mathrm{d}k_\rho\, \mathrm{d}p \tag{72}$$

We find that this corresponds to a continuous line of point sources in complex z space, where $f(p)$ is related to the image current function.

$$A_2(\mathbf{r}) = \int\limits_0^\infty f(p) G\left(\mathbf{r} + \left(h + \frac{p}{ik\sqrt{\varepsilon-1}}\right)\hat{\mathbf{z}}\right) \mathrm{d}p \tag{73}$$

Expressing this in more physically explicit quantities,

$$A_2(\mathbf{r}) = \int\limits_{-h}^{-\infty e^{i\theta}} I(z') G(\mathbf{r} - z'\hat{\mathbf{z}}) \mathrm{d}z' \tag{74}$$

where

$$\theta = -\arg(i\sqrt{\varepsilon-1}) \tag{75}$$

$$z' = -h - \frac{p}{ik\sqrt{\varepsilon-1}} \tag{76}$$

$$I(z') = -ik\sqrt{\varepsilon-1} f\left(-ik\sqrt{\varepsilon-1}(z'+h)\right) \tag{77}$$

The line of point sources exist along z', and $I(z')$ is the magnitude of the current along that line.

Now, if we know $f(p)$ we may simply substitute in (74), and find the net vector potential by superposition of the image point sources.

$f(p)$ is simply the Laplace transform of $R_e(q)$. One of the forms of $f(p)$ is

$$f(p) = \frac{\varepsilon-1}{\varepsilon+1}\delta(p) - \varepsilon\gamma \frac{\varepsilon-1}{\varepsilon+1} \sinh(\gamma p) + 2\varepsilon\gamma \int\limits_0^p \sinh\left[\gamma(p-s)\right] \frac{J_2(s)}{s} \mathrm{d}s \tag{78}$$

where

$$\gamma = \frac{1}{\sqrt{\varepsilon^2-1}} \tag{79}$$

More numerically suitable forms of $f(p)$ are derived using various approximations in [14]. These approximations result in the series forms (80) and (81) for $f(p)$.

For $p < 4$,

$$f(p) = \frac{\varepsilon-1}{\varepsilon+1}\delta(p) + \sum_{n=0}^\infty \left[-\varepsilon\gamma \frac{\varepsilon-1}{\varepsilon+1} + \varepsilon \sum_{m=0}^{n-1} \frac{(-1)^m(2m+1)!}{(2\gamma)^{2m+1}m!(m+2)!}\right] \frac{(\gamma p)^{2n+1}}{(2n+1)!} \tag{80}$$

For $p > 4$,

$$f(p) = -2\varepsilon^2\gamma^3 e^{-\gamma p} + \frac{2\sqrt{2}}{\varepsilon\sqrt{\pi} p^{\frac{3}{2}}} \sin\left(p + \frac{\pi}{4}\right) + \frac{3(8-3\varepsilon^2)}{2\varepsilon^3\sqrt{2\pi} p^{\frac{5}{2}}} \cos\left(p + \frac{\pi}{4}\right) + \cdots \tag{81}$$

These expressions can finally be used to compute the net effect of all the image sources using numerical integration of (74).

Exact image theory provides an alternative way to understand the reflection as arising from a set of point sources. But note that these sources are positioned along a line in the complex plane and this may not have an apparent physical interpretation. Our analysis presented in Section 7 shows that the cost of computation using this approach may be higher than the contour integration, for ρ and $z + h$ values less than λ. It is clear that as ρ increases, the computational cost of contour integration with the Bessel function form of the integrand increases due to the increased oscillation of the integrand. Therefore, exact image theory could potentially be exploited for mesoscale problems.

6. Fourier expansion of the reflection coefficient

This technique approximates the reflection coefficient part of the Sommerfeld integral using a Fourier series. The resulting series of integrals is analytically integrable, thus converting the problem to a series summation.

We start with a Sommerfeld integral of the form

$$A_z = \int\limits_0^\infty J_0(k_\rho \rho) e^{-k_z(z+h)} \left[\frac{\varepsilon k_z}{\varepsilon k_z + k_{zs}} \right] \frac{k_\rho}{k_z} dk_\rho \tag{82}$$

The bracketed part is the reflection coefficient and is slowly varying with respect to the variable of integration and will be approximated using a Fourier series.

Changing integration variables by substituting $k_\rho = k \sin\alpha$ and therefore $k_z = \sqrt{k_\rho^2 - k^2} = ik \cos\alpha$, we get

$$A_z = L + T \tag{83}$$

where

$$L = k \int\limits_0^{\frac{\pi}{2}} S_L(\cos\alpha) J_0(k\rho \sin\alpha) e^{-k \cos\alpha[\delta + i(z+h)]} \sin\alpha d\alpha \tag{84}$$

$$T = k \int\limits_{\frac{\pi}{2}}^{\frac{\pi}{2}+j\infty} S_T(i \cos\alpha) J_0(k\rho \sin\alpha) e^{-ik \cos\alpha(z+h)} \sin\alpha d\alpha \tag{85}$$

$$S_L(\psi) = \frac{\varepsilon \psi e^{k\psi\delta}}{\varepsilon\psi + \sqrt{\varepsilon - 1 + \psi^2}} \tag{86}$$

$$S_T(\psi) = \frac{\varepsilon\psi}{\varepsilon\psi + i\sqrt{\varepsilon - 1 + \psi^2}} \tag{87}$$

Making a further substitution, $\psi = \cos\alpha$ in (84) and $\psi = i\cos\alpha$ in (85), we get

$$L = -ik \int\limits_0^1 S_L(\psi) J_0(k\rho\sqrt{1 - \psi^2}) e^{-k\psi[\delta + i(z+h)]} d\psi \tag{88}$$

$$T = k \int\limits_0^\infty S_T(\psi) J_0(k\rho\sqrt{1 + \psi^2}) e^{-k\psi(z+h)} d\psi \tag{89}$$

Now, we approximate the slowly varying parts of the integral namely $S_L(\psi)$ and $S_T(\psi)$ using a Fourier series as follows.

Integral for L in (88) has finite limits $0 \leq \psi \leq 1$. So, S_L can be approximated by extending it as an even function about $\psi = 1$, and then approximating it using an N_L point Fourier sine transform.

$$s_L(v) = \sum_{\psi=1}^{N_L-1} S_L(\psi) \sin\left(\pi \frac{\psi}{\Delta\psi} \frac{v}{N_L}\right) \tag{90}$$

$$S_L(\psi) = \frac{2}{N_L} \sum_{v=1,\, v\,odd}^{N_L-1} s_L(v) \sin\left(\pi \frac{\psi}{\Delta\psi} \frac{v}{N_L}\right) \tag{91}$$

where $\Delta\psi = \frac{2}{N_L}$.

Integral for T in (89) has infinite limits. Therefore, the integral needs to be truncated at some ψ_{max}, before S_T can be approximated using a Fourier series. ψ_{max} is chosen to be a point where the exponential function in the integral would have decayed to a very small value and therefore the contribution of the integral for $\psi > \psi_{max}$ can be neglected.

ψ_{max} is chosen to be

$$\psi_{max} = -\frac{1}{kz_{min}} \ln\left(0.5 \times 10^{-(SD+2)}\right) \tag{92}$$
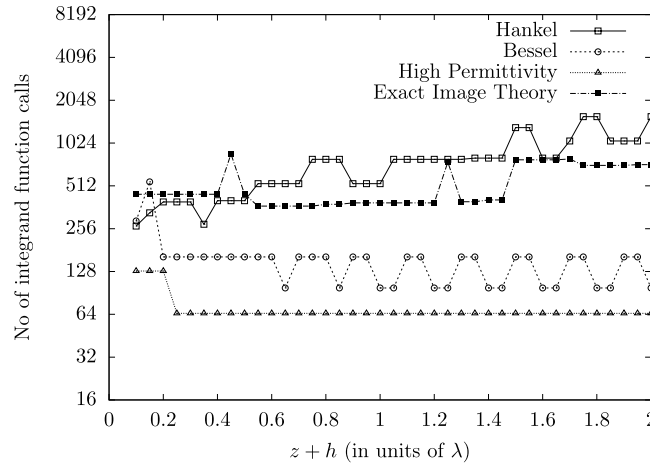
Fig. 9. Comparison of computational costs involved in the various methods (for parameters $k = 1$, $\varepsilon = 7 + 3i$, $\rho = 0.15\lambda$). Integration contours used for the data points marked "Bessel", "Hankel" and "High Permittivity" are shown as dashed lines in Figs. 1, 4 and 6 respectively. Romberg quadrature to a relative tolerance of 10^{-6} was used to numerically evaluate all integrals.

where SD is the number of significant digits accuracy required, and z_{min} is the minimum $z + h$ for which the Fourier series approximation will be used.

Extending S_T as an even function about $\psi = \psi_{max}$, we get

$$s_T(\nu) = \sum_{\psi=1}^{N_T-1} S_T(\psi) \sin\left(\pi \frac{\psi}{\Delta\psi} \frac{\nu}{N_T}\right) \qquad (93)$$

$$S_T(\psi) = \frac{2}{N_T} \sum_{\nu=1,\,\nu\,odd}^{N_T-1} s_T(\nu) \sin\left(\pi \frac{\psi}{\Delta\psi} \frac{\nu}{N_T}\right) \qquad (94)$$

Substituting the Fourier series approximations developed above back into (88) and (89), makes the integrals analytically integrable. Expressions for the results after analytical integration are available in [5].

The slowly varying parts of the integral S_L and S_T are parameterized only by the permittivity of the surface, and is independent of the positions of the source and observation points. Hence, for a given surface, the Fourier series approximations need to be computed only once and can be used repeatedly for various source and observation points, thus saving on computation. However, for observation points close to the surface, the convergence is slow, and a large number of sample points need to be used in the Fourier series approximation [5]. This is problematic and any computational advantage gained over numerical integration of the Sommerfeld integral may be lost here.
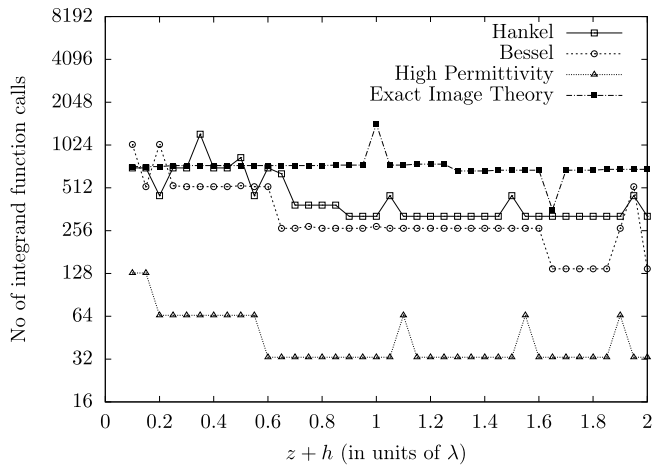
7. Comparison of computational cost

In this section, we compare the computational cost of the various methods used to evaluate the Sommerfeld integral. In the case of contour integration, exact image theory and the high permittivity approximation, the number of integrand evaluations has been chosen as a measure of the computational cost. For exact image theory, since the series calculations for $f(p)$ involve double summations, the number of terms in the series has also been added to the number of integrand evaluations performed during numerical integration. For the short distance approximation, only analytical expressions are involved, the cost of which is negligibly small compared to numerical integration. Hence we ignore it here. But note that its region of validity is limited as described in Section 4.

The various methods of computation have different integrands each with their distinct computational costs. Therefore, the cost involved with a single integrand evaluation is not the same for different methods. However, this simplistic scheme assuming that all integrand and series evaluations are equivalent was chosen in order to decouple the measurement of computational cost from exact implementation details such as choice of numerical integration methods, choice of math libraries, compiler optimization, etc.

Figs. 9, 10 and 11 show a comparison of the number of integrand evaluations required for convergence in each method for different ρ and $z + h$. Romberg quadrature to a relative tolerance of 10^{-6} was used to numerically evaluate all integrals. The integrals were truncated to finite limits such that the envelope of the integrand decays to a negligible value ($e^{-k_z(z+h)} \approx 10^{-16}$) close to machine epsilon at the upper limit. For example, in contour integration with Bessel functions, $\frac{1-i}{\rho} + \frac{40}{z+h}$ was chosen as the upper limit of k_ρ along the path shown in Fig. 1. With such a limit, the accuracy of the numerical integration is dependent primarily on the relative tolerance requirement placed on the quadrature scheme. From the figures, we can
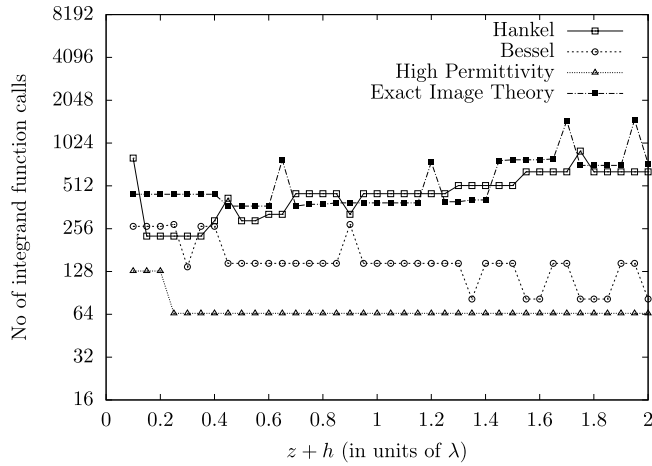
Fig. 10. Comparison of computational costs involved in the various methods (for parameters $k = 1$, $\varepsilon = 7 + 3i$, $\rho = 0.35\lambda$). Integration contours used for the data points marked "Bessel", "Hankel" and "High Permittivity" are shown as dashed lines in Figs. 1, 4 and 6 respectively. Romberg quadrature to a relative tolerance of 10^{-6} was used to numerically evaluate all integrals.

Fig. 11. Comparison of computational costs involved in the various methods (for parameters $k = 1$, $\varepsilon = 7 + 3i$, $\rho = 2\lambda$). Integration contours used for the data points marked "Bessel", "Hankel" and "High Permittivity" are shown as dashed lines in Figs. 1, 4 and 6 respectively. Romberg quadrature to a relative tolerance of 10^{-6} was used to numerically evaluate all integrals.

see that the high permittivity approximation shows the lowest cost. But, as we saw earlier, its accuracy is too poor to be practically useful. Contour integration has an order of magnitude lower computational cost than exact image theory for $z + h$ on the order of λ. But, when the observation point tends to the far field, they are observed to be closely matched. Among the contour integrations, the Bessel function form of the integrand is slightly inferior to the Hankel function form for very low $z + h$, but at larger $z + h$, the increased exponential decay due to the large $z + h$ gives the Bessel function form of the integrand an advantage.

Appendix A. Domain coloring for visualizing complex functions

Domain coloring is a technique for visualizing complex functions. Representing a complex function with separate magnitude and phase plots makes it difficult to put together and interpret. In domain coloring, the magnitude and phase of the complex function are mapped respectively to the value (V) and hue (H) components of that point in the HSV color space. The saturation (S) component of the color is set constant to unity. Thus, oscillations (that is, phase change) in the function are represented by changes in hue (color), and magnitude is represented by the brightness. Darker shades represent smaller magnitude, and brighter shades represent larger magnitude.

For the domain coloring visualizations shown in Figs. 2 and 5, the chosen mapping of the complex number to the color was

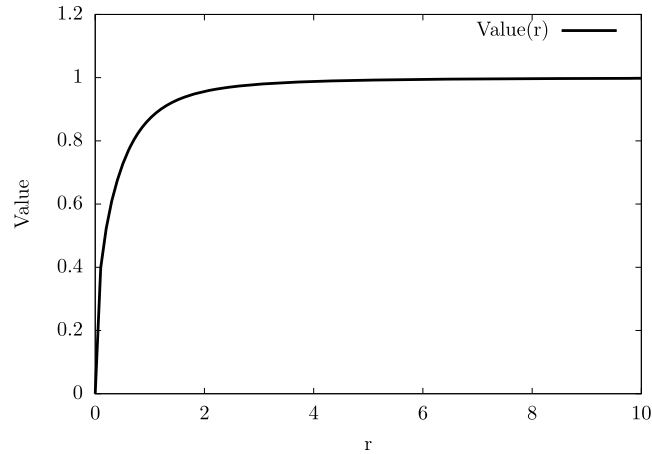$$\text{Hue}(re^{i\phi}) = \phi \tag{A.1}$$

Fig. 12. Mapping of magnitude to Value (V) used in the domain coloring visualizations.

$$\text{Saturation}(re^{i\phi}) = 1 \tag{A.2}$$

$$\text{Value}(re^{i\phi}) = \left(1 - \frac{1}{1+r^2}\right)^{0.2} \tag{A.3}$$

where r and ϕ are the magnitude and phase of the complex number respectively.

The mapping of magnitude (r) to the Value (V) component of the HSV color is shown in Fig. 12. In the HSV color space, the maximum allowed value of the Value (V) component is 1. Hence the mapping is chosen such that it saturates for large magnitudes and does not exceed 1.

Appendix B. Branch cuts of the Sommerfeld integrand

B.1. Branch cuts due to $\sqrt{k_\rho^2 - k^2}$

Letting $k_\rho = x + iy$, where x and y are the real and imaginary parts of k_ρ respectively,

$$k_\rho^2 - k^2 = (x^2 - y^2 - k^2) + i2xy \tag{B.1}$$

For the conventional principal value of the square root function, the branch cuts in the k_ρ plane satisfy

$$\Re\{k_\rho^2 - k^2\} < 0, \quad \Im\{k_\rho^2 - k^2\} = 0 \tag{B.2}$$

Thus,

$$x^2 - y^2 - k^2 < 0 \tag{B.3a}$$

$$2xy = 0 \tag{B.3b}$$

From (B.3b), $x = 0$ or $y = 0$.

If $x = 0$, from (B.3a),

$$y^2 > -k^2 \tag{B.4}$$

Since y and k are real numbers, y^2 is always positive and $-k^2$ is always negative for all y, k, making the above inequality true for all $y \in \mathbb{R}$. Thus, there exists an infinitely long branch cut along the imaginary axis in the k_ρ plane. This can be mathematically expressed as

$$k_\rho = it, \quad t \in \mathbb{R} \tag{B.5}$$

If $y = 0$, from (B.3a),

$$x^2 < k^2 \implies |x| < |k| \tag{B.6}$$

Since k is real and positive, $|x| < k$. Thus, the branch cut is

$$k_\rho = t, \quad t \in [-k, k] \tag{B.7}$$

B.2. Branch cuts due to $\sqrt{k_\rho^2 - \varepsilon k^2}$

Letting $k_\rho = x + iy$, where x and y are the real and imaginary parts of k_ρ respectively, and $\varepsilon = \varepsilon_x + i\varepsilon_y$, where ε_x and ε_y are the real and imaginary parts of ε respectively,

$$k_\rho^2 - \varepsilon k^2 = (x^2 - y^2 - \varepsilon_x k^2) + i(2xy - \varepsilon_y k^2) \tag{B.8}$$

For the conventional principal value of the square root function, the branch cuts in the k_ρ plane satisfy

$$\Re\{k_\rho^2 - \varepsilon k^2\} < 0, \quad \Im\{k_\rho^2 - \varepsilon k^2\} = 0 \tag{B.9}$$

Thus,

$$x^2 - y^2 - \varepsilon_x k^2 < 0 \tag{B.10a}$$
$$2xy - \varepsilon_y k^2 = 0 \tag{B.10b}$$

From (B.10b),

$$y = \frac{\varepsilon_y k^2}{2x} \tag{B.11}$$

Substituting in (B.10a),

$$x^4 - \varepsilon_x k^2 x^2 - \frac{\varepsilon_y^2 k^4}{4} < 0 \tag{B.12}$$

Completing squares,

$$\left(x^2 - \frac{\varepsilon_x k^2}{2}\right)^2 < \frac{k^4}{4}\left(\varepsilon_x^2 + \varepsilon_y^2\right) \tag{B.13}$$

$$\left(x^2 - \frac{\varepsilon_x k^2}{2}\right)^2 < \frac{k^4 |\varepsilon|^2}{4} \tag{B.14}$$

Thus,

$$-\frac{|\varepsilon|k^2}{2} < x^2 - \frac{\varepsilon_x k^2}{2} < \frac{|\varepsilon|k^2}{2} \tag{B.15}$$

$$\frac{(\varepsilon_x - |\varepsilon|)k^2}{2} < x^2 < \frac{(\varepsilon_x + |\varepsilon|)k^2}{2} \tag{B.16}$$

But,

$$|\varepsilon| = \sqrt{\varepsilon_x^2 + \varepsilon_y^2} \tag{B.17}$$

Therefore,

$$|\varepsilon| \geq \varepsilon_x \tag{B.18}$$

This means that $\varepsilon_x - |\varepsilon|$ is negative. But, x is real, and so x^2 is always positive. Therefore, $x^2 > (\varepsilon_x - |\varepsilon|)\frac{k^2}{2}$ is always satisfied. This leaves us with the condition,

$$x^2 > (\varepsilon_x + |\varepsilon|)\frac{k^2}{2} \tag{B.19}$$

But,

$$\Re\{\sqrt{\varepsilon}\} = \sqrt{|\varepsilon|}\cos\left(\frac{1}{2}\arg\varepsilon\right) \tag{B.20}$$

$$[\Re\{\sqrt{\varepsilon}\}]^2 = |\varepsilon|\cos^2\left(\frac{1}{2}\arg\varepsilon\right) \tag{B.21}$$

$$[\Re\{\sqrt{\varepsilon}\}]^2 = \frac{|\varepsilon|}{2}[1 + \cos(\arg\varepsilon)] \tag{B.22}$$

$$[\Re\{\sqrt{\varepsilon}\}]^2 = \frac{|\varepsilon|}{2}\left[1 + \frac{\varepsilon_x}{|\varepsilon|}\right] \tag{B.23}$$

$$[\Re\{\sqrt{\varepsilon}\}]^2 = \frac{\varepsilon_x + |\varepsilon|}{2} \tag{B.24}$$

Substituting in (B.19),

$$x^2 > k^2 [\Re\{\sqrt{\varepsilon}\}]^2 \tag{B.25}$$

Thus, the branch cut exists for

$$-k\Re\{\sqrt{\varepsilon}\} < x < k\Re\{\sqrt{\varepsilon}\} \tag{B.26}$$

From (B.11), the branch cut is

$$k_\rho = t + i\frac{\varepsilon_y k^2}{2t}, \quad t \in \left[-k\Re\{\sqrt{\varepsilon}\}, k\Re\{\sqrt{\varepsilon}\}\right] \tag{B.27}$$

Appendix C. Branch cuts of the high permittivity integrand

The high permittivity integrand shown in (19) has branch cuts due to the square root function in

$$R'' = \sqrt{\rho^2 + (z+h')^2} \tag{C.1}$$

Letting $z' = \sqrt{x^2 + y^2}$ where x and y are the real and imaginary parts of z' respectively,

$$\rho^2 + z'^2 = \rho^2 + x^2 - y^2 + i2xy \tag{C.2}$$

For the conventional principal value of the square root function, the branch cuts in the z' plane satisfy

$$\Re\{\rho^2 + z'^2\} < 0, \quad \Im\{\rho^2 + z'^2\} = 0 \tag{C.3}$$

Thus,

$$\rho^2 + x^2 - y^2 < 0 \tag{C.4}$$

$$2xy = 0 \tag{C.5}$$

From (C.5), $x = 0$ or $y = 0$. If $x = 0$, from (C.4),

$$y^2 > \rho^2 \implies |y| > \rho \tag{C.6}$$

If $y = 0$, from (C.4),

$$x^2 < -\rho^2 \tag{C.7}$$

Since x is a real number, x^2 is always positive. Since ρ is a real number, $-\rho^2$ is always negative. Therefore, the above condition is not possible for any real x.

Therefore, the branch cut is given by

$$z' = \pm it, \quad t \in [\rho, \infty) \tag{C.8}$$

References

[1] B.K. Alpert, Hybrid Gauss-trapezoidal quadrature rules, SIAM J. Sci. Comput. 20 (5) (1999) 1551–1584.
[2] A. Barnett, L. Greengard, A new integral representation for quasi-periodic fields and its application to two-dimensional band structure calculations, J. Comput. Phys. 229 (19) (2010) 6898–6914.
[3] O.P. Bruno, L.A. Kunyansky, A fast, high-order algorithm for the solution of surface scattering problems: basic implementation, tests, and applications, J. Comput. Phys. 169 (1) (2001) 80–110.
[4] G.J. Burke, E.K. Miller, Modeling antennas near to and penetrating a lossy interface, IEEE Trans. Antennas Propag. 32 (10) (1984) 1040–1049.
[5] S.L. Dvorak, Application of the fast Fourier transform to the computation of the Sommerfeld integral for a vertical electric dipole above a half-space, IEEE Trans. Antennas Propag. 40 (7) (1992) 798–805.
[6] V.V. Gozhenko, L.G. Grechko, K.W. Whites, Electrodynamics of spatial clusters of spheres: substrate effects, Phys. Rev. B 68 (12) (2003) 125422.
[7] J. Helsing, Integral equation methods for elliptic problems with boundary conditions of mixed type, J. Comput. Phys. 228 (23) (2009) 8892–8907.
[8] T.R. Jensen, M.D. Malinsky, C.L. Haynes, R.P. Van Duyne, Nanosphere lithography: tunable localized surface plasmon resonance spectra of silver nanoparticles, J. Phys. Chem. B 104 (45) (2000) 10549–10556.
[9] S. Kapur, V. Rokhlin, High-order corrected trapezoidal quadrature rules for singular functions, SIAM J. Numer. Anal. 34 (4) (1997) 1331–1356.
[10] M.W. Knight, Y. Wu, J.B. Lassiter, P. Nordlander, N.J. Halas, Substrates matter: influence of an adjacent dielectric on an individual plasmonic nanoparticle, Nano Lett. 9 (5) (2009) 2188–2192.
[11] J. Lermé, C. Bonnet, M. Broyer, E. Cottancin, D. Manchon, M. Pellarin, Optical properties of a particle above a dielectric interface: cross sections, benchmark calculations, and analysis of the intrinsic substrate effects, J. Phys. Chem. C 117 (12) (2013) 6383–6398.
[12] P.A. Letnes, I. Simonsen, D. Mills, Substrate influence on the plasmonic response of clusters of spherical nanoparticles, Phys. Rev. B 83 (7) (2011) 075426.
[13] I.V. Lindell, E. Alanen, Exact image theory for the Sommerfeld half-space problem, part I: vertical magnetic dipole, IEEE Trans. Antennas Propag. AP-32 (2) (February 1984).

[14] I.V. Lindell, E. Alanen, Exact image theory for the Sommerfeld half-space problem, part II: vertical electric dipole, IEEE Trans. Antennas Propag. AP-32 (8) (August 1984).

[15] I.V. Lindell, E. Alanen, Exact image theory for the Sommerfeld half-space problem, part III: general formulation, IEEE Trans. Antennas Propag. AP-32 (10) (October 1984).

[16] R.J. Lytle, D.L. Lager, Numerical evaluation of Sommerfeld integrals, Technical report, Lawrence Livermore Laboratories, 1974.

[17] S.Z. Malynych, N.L. Dmitruk, I.E. Moroz, Influence of substrate on the optical properties of non-aggregated silver nanoparticles, Eur. Phys. J. Appl. Phys. 64 (02) (2013) 20402.

[18] G.Y. Panasyuk, J.C. Schotland, V.A. Markel, Short-distance expansion for the electromagnetic half-space green's tensor: general results and an application to radiative lifetime computations, J. Phys. A, Math. Theor. 42 (27) (2009) 275203.

[19] R. Schmehl, B.M. Nebeker, E.D. Hirleman, Discrete-dipole approximation for scattering by features on surfaces by means of a two-dimensional fast Fourier transform technique, J. Opt. Soc. Am. A 14 (11) (1997) 3026–3036.

[20] A. Sommerfeld, Über die ausbreitung der wellen in der drahtlosen telegraphie, Ann. Phys. 333 (4) (1909) 665–736.

[21] A. Sommerfeld, Über die ausbreitung der wellen in der drahtlosen telegraphie, Ann. Phys. 386 (25) (1926) 1135–1153.

[22] A. Sommerfeld, Partial Differential Equations, Academic Press, 1949, pp. 246–267, chapter 6.

[23] P. Valle, E. Ortiz, J. Saiz, Near field by subwavelength particles on metallic substrates with cylindrical surface plasmon excitation, Opt. Commun. 137 (4) (1997) 334–342.

[24] M. Venkatapathi, A.K. Tiwari, Radiative and non-radiative effects of a substrate on localized plasmon resonance of particles, J. Appl. Phys. 112 (1) (2012) 013529.

[25] K.C. Vernon, A.M. Funston, C. Novo, D.E. Gómez, P. Mulvaney, T.J. Davis, Influence of particle–substrate interaction on localized plasmon resonances, Nano Lett. 10 (6) (2010) 2080–2086.

[26] Y. Wu, P. Nordlander, Finite-difference time-domain modeling of the optical properties of nanoparticles near dielectric substrates, J. Phys. Chem. C 114 (16) (2009) 7302–7307.

[27] G. Xu, Y. Chen, M. Tazawa, P. Jin, Influence of dielectric properties of a substrate upon plasmon resonance spectrum of supported Ag nanoparticles, Appl. Phys. Lett. 88 (4) (2006) 043114.

[28] J. Yan, K.S. Thygesen, K.W. Jacobsen, Nonlocal screening of plasmons in graphene by semiconducting and metallic substrates: first-principles calculations, Phys. Rev. Lett. 106 (14) (2011) 146803.